Eur. Phys. J. D **8**, 417–429 (2000)

THE EUROPEAN PHYSICAL JOURNAL D

EDP Sciences

Bistable behaviour in squeezed vacua: II. Stability analysis and chaos

H.A. Batarfi[1], S.S. Hassan[2], R. Saunders[3], and R.K. Bullough[4]

[1] King Abdul-Aziz University, Faculty of Science, Mathematics Department (Women's Section), P.O. Box 41101, Jeddah 21521, Saudi Arabia
[2] Ain Shams University, Faculty of Science, Mathematics Department, Cairo, Egypt
[3] Department of Mathematics and Physics, Manchester Metropolitan University, Manchester M1 5GD, England
[4] UMIST, Mathematics Department, P.O. Box 88, Manchester M60 1QD, England

Received 12 March 1999 and Received in final form 20 August 1999

Abstract. Linear stability analysis and (numerical) investigation of the periodic and chaotic self-pulsing behaviour are presented for the Maxwell-Bloch equations of a bistable model in contact with a squeezed vacuum field. Effect of the squeeze phase parameter on the period doubling bifurcation that preceeds chaos is examined for the adiabatic and non-adiabatic regimes.

PACS. 42.65.Pc Optical bistability, multistability, and switching – 42.65.Sf Dynamics of nonlinear optical systems; optical instabilities, optical chaos and complexity, optical spatio-temporal dynamics

1 Introduction

As seen in Part I of this paper [1] the input-output nonlinear relationship $y = f(x)$ (y is the (real) input field amplitude and x is the output field amplitude) of a bistable system is represented by an S-shape curve of three branches in which the intermediate branch has a negative slope where $\mathrm{d}|x|/\mathrm{d}y < 0$, *i.e.* unstable. However, it is not true that branches of positive slope where $\mathrm{d}|x|/\mathrm{d}y > 0$ are always stable. This was first shown, theoretically and experimentally, by McCall [2] in a hybrid bistable device where a cw laser input was converted into a train of light pulses. Subsequently Bonifacio and Lugiato [3] and Bonifacio *et al.* [4] gave linear stability analysis for an absorptive optical bistability (OB) system (in normal vacuum) in a ring cavity and showed that, under certain conditions, part of the positive slope (upper) branch of the OB curve is unstable. The analysis was later generalized to the dispersive case [5] (also see [6] and references therein).

In this Part II, we present a linear stability analysis and investigate the self-pulsing and chaotic behaviour of the bistable model in a squeezed vacuum considered in [1] in both cases of the absorptive and dispersive OB.

2 Stability analysis

2.1 Absorptive case

Without early adoption of the (spatial) mean field limit (*cf.* [1]) the stationary solutions of the model equations (Eqs. (2b, 2c)) of [1] for the matter variables are space-dependent and are given in the absorptive case ($\delta = \theta = 0$) by (we put $g = \gamma/(2\sqrt{2})$ for direct comparison with [2,3])

$$J_z^{\mathrm{st}}(z) = -\frac{\gamma}{2\gamma_\parallel}\left[1 + b_1(z)|\alpha^{\mathrm{st}}(z)|^2\right]^{-1}, \tag{1a}$$

$$\begin{aligned} J_-^{\mathrm{st}}(z) &= -\frac{\sqrt{2}}{\gamma_\parallel}\left[1 + b_1(z)|\alpha^{\mathrm{st}}(z)|^2\right]^{-1} \\ &\quad \times \left[G_o\alpha^{\mathrm{st}}(z) - \gamma M\left(\alpha^{\mathrm{st}}(z)\right)^*\right] \\ &= (J_+^{\mathrm{st}}(z))^* \end{aligned} \tag{1b}$$

where $G_o = (\gamma/2)(1 + 2N)$ and $b_1(z) = 1 - 2|M|\cos(\phi(z))/(1 + 2N)$, whilst the stationary solution for the field (Eq. (2a) of [1]) is given by

$$c\frac{\mathrm{d}\alpha^{\mathrm{st}}(z)}{\mathrm{d}z} = -\frac{\gamma}{2\sqrt{2}}J_-^{\mathrm{st}}(z). \tag{1c}$$

To study the stability of the stationary solutions we introduce the small deviations $\delta\alpha$ and $\delta J_{\pm,z}$

$$\begin{aligned} \alpha(z,t) &= \delta\alpha(z,t) + \alpha^{\mathrm{st}}(z) \\ J_-(z,t) &= \delta J_-(z,t) + J_-^{\mathrm{st}}(z) = (J_+(z,t))^* \\ J_z(z,t) &= \delta J_z(z,t) + J_z^{\mathrm{st}}(z) \end{aligned} \tag{2}$$

where the boundary conditions (*cf.* Eqs. (1) of [1]) for $\delta\alpha(z,t)$ now reads (for $\theta = 0$),

$$\delta\alpha(0,t) = (1-T)\delta\alpha(L\ , t - \Delta t). \tag{3}$$

By substituting equations (2) into equations (1) and discarding the bilinear terms in $(\delta\alpha\ \delta J_\pm)$ and $(\delta\alpha\ \delta J_z)$ we get the following set of the linearized equations for the deviations

$$\begin{aligned}\frac{\partial}{\partial t}\left(\delta J_z(z,t)\right) &= -\gamma_\parallel \delta J_z(z,t) - \frac{\gamma}{2\sqrt{2}}\left[\alpha^{\rm st}(z)\delta J_+(z,t)\right.\\ &\quad +(\alpha^{\rm st}(z))^*\delta J_-(z,t) + J_-^{\rm st}(z)\delta\alpha^*(z,t)\\ &\quad \left.+J_-^{\rm st}(z)\delta\alpha(z,t)\right] \qquad (4a)\\ \frac{\partial}{\partial t}\left(\delta J_-(z,t)\right) &= -G\delta J_-(z,t) + \frac{\gamma}{\sqrt{2}}\left[\alpha^{\rm st}(z)\delta J_z(z,t)\right.\\ &\quad \left.+J_z^{\rm st}(z)\delta\alpha(z,t)\right] - \gamma M\delta J_+(z,t)\\ &= \left[\frac{\partial}{\partial t}\left(\delta J_+(z,t)\right)\right]^* \qquad (4b)\\ \frac{\partial}{\partial t}\left(\delta\alpha(z,t)\right) + c\frac{\partial}{\partial z}\left(\delta\alpha(z,t)\right) &= -\frac{\gamma}{2\sqrt{2}}\,\delta J_-(z,t). \qquad (4c)\end{aligned}$$

Now we look for solutions of equations (4) in the form

$$\begin{aligned}\delta\alpha^\lambda(z,t) &= \delta\alpha^\lambda(z)\exp(\lambda t) + c.c.\\ \delta J_z^\lambda(z,t) &= \delta J_z^\lambda(z)\exp(\lambda t) + c.c.\\ \delta J_-^\lambda(z,t) &= \delta J_-^\lambda(z)\exp(\lambda t) + c.c. \qquad (5)\end{aligned}$$

Hence from equations (4, 5) one gets the following equation for the field deviation $\delta\alpha^\lambda(z)$,

$$\begin{aligned}\frac{\mathrm{d}}{\mathrm{d}z}\left(\delta\alpha^\lambda(z)\right) &= \left[B(z)-\lambda/c\right]\delta\alpha^\lambda(z) + D(z)\left[\delta\alpha^\lambda(z)\right]^*\\ &= \left[\frac{\mathrm{d}}{\mathrm{d}z}(\delta\alpha^\lambda(z))^*\right]^* \qquad (6)\end{aligned}$$

where

$$\begin{aligned}B(z) &= -\Omega_1\left\{(\lambda+G_o)J_z^{\rm st} - \Omega_2\Big[\frac{\gamma}{2\sqrt{2}}J_+^{\rm st}\right.\\ &\quad \left.+\Omega_3\left[(\lambda+G_o)(\alpha^{\rm st})^* - \gamma M^*\alpha^{\rm st}\right]\Big]\right\}, \qquad (7a)\\ D(z) &= \Omega_1\left\{\gamma M\ J_z^{\rm st} + \Omega_2\Big[\frac{\gamma}{2\sqrt{2}}J_-^{\rm st}\right.\\ &\quad \left.+\Omega_3\left[(\lambda+G_o)\alpha^{\rm st} - \gamma M(\alpha^{\rm st})^*\right]\Big]\right\} \qquad (7b)\end{aligned}$$

with

$$\begin{aligned}\Omega_1 &= \frac{\gamma^2}{4c}(|\lambda+G_o|^2-\gamma^2|M|^2)^{-1},\\ \Omega_2 &= \left[(\lambda+G_o)\alpha^{\rm st} - \gamma M(\alpha^{\rm st})^*\right]\\ &\quad\times\left[\lambda+\gamma_\parallel+\frac{\gamma^2}{4}|\alpha^{\rm st}|^2\frac{2\lambda+\gamma(1+2N)b_1(z)}{|\lambda+G_o|^2-\gamma^2|M|^2}\right]^{-1},\\ \Omega_3 &= \frac{\gamma^2}{4}\frac{J_z^{\rm st}}{|\lambda+G_o|^2-\gamma^2|M|^2}, \qquad (7c)\end{aligned}$$

$\alpha^{\rm st} \equiv \alpha^{\rm st}(z)$ and $J_{z,\pm}^{\rm st} \equiv J_{z,\pm}^{\rm st}(z)$ are given by equations (1a, 1b). Within the mean field limit, the quantities $B(z)$, $D(z)$ in (7) are replaced by their values at $z = L$, *i.e.* $\alpha^{\rm st}(z)$ is replaced by $\alpha^{\rm st}(L)$. Thus equation (6) reduce to the coupled differential equations with constant coefficients

$$\begin{aligned}\frac{\mathrm{d}}{\mathrm{d}z}\left(\delta\alpha^\lambda(z)\right) &=\\ &\left(B(L)-\lambda/c\right)\delta\alpha^\lambda(z) + D(L)\left(\delta\alpha^\lambda(z)\right)^* \qquad (8a)\\ \frac{\mathrm{d}}{\mathrm{d}z}\left(\delta\alpha^\lambda(z)\right)^* &=\\ &\left(B^*(L)-\lambda/c\right)\left(\delta\alpha^\lambda(z)\right)^* + D^*(L)\delta\alpha^\lambda(z). \qquad (8b)\end{aligned}$$

Note that in the present squeezed vacuum case the deviation $\delta\alpha^\lambda(z)$ is *coupled* to its complex conjugate $(\delta\alpha^\lambda(z))^*$ unlike the situation in the normal vacuum case (*cf.* [3]). The solutions of (8) are given by

$$\begin{aligned}\delta\alpha^\lambda(z) &= \xi_1(L)\exp\left[\left(\beta_1(L)+\mathrm{i}\beta_2(L)\right)z\right]\\ &\quad +\xi_2(L)\exp\left[\left(\beta_1(L)-\mathrm{i}\beta_2(L)\right)z\right]\\ &= \left[\left(\delta\alpha^\lambda(z)\right)^*\right]^* \qquad (9)\end{aligned}$$

where

$$\begin{aligned}\xi_1(L) &= \frac{1}{2}\delta\alpha^\lambda(0) - \frac{\mathrm{i}}{2\overline{\beta}_2}\Big[\frac{1}{2}(\overline{C}_1-\overline{C}_1^*)\delta\alpha^\lambda(0)\\ &\quad +\overline{D}\left(\delta\alpha^\lambda(0)\right)^*\Big],\\ \xi_2(L) &= \frac{1}{2}\delta\alpha^\lambda(0) + \frac{\mathrm{i}}{2\overline{\beta}_2}\Big[\frac{1}{2}(\overline{C}_1-\overline{C}_1^*)\delta\alpha^\lambda(0)\\ &\quad +\overline{D}\left(\delta\alpha^\lambda(0)\right)^*\Big], \qquad (10a)\\ \beta_1(L) &= \mathrm{Re}(C_1),\\ \beta_2(L) &= \frac{\gamma}{2}\left[|\overline{C}_1|^2 - |\overline{D}|^2 - \frac{1}{4}\left(\overline{C}_1+\overline{C}_1^*\right)^2\right]^{1/2},\\ C_1 &= B(L)-\lambda/c, \quad \overline{C}_1 = \frac{c}{\gamma}C_1 = \overline{B}(L)-\overline{\lambda} \qquad (10b)\end{aligned}$$

and the dimensionless variables $\overline{B}(L), \overline{D}(L)$ and $\overline{\lambda}$ are given by $(cB(L)/\gamma)$, $(cD(L)/\gamma)$, and (λ/γ) respectively.

Multiplying (9) by $\mathrm{e}^{\lambda t}$ and in view of (5) we get,

$$\begin{aligned}\delta\alpha^\lambda(z,t) &= \mathrm{e}^{\lambda t}\left\{\xi_1(L)\exp\left[\frac{\gamma z}{c}\left(\overline{\beta}_1(L)+\mathrm{i}\overline{\beta}_2(L)\right)\right]\right.\\ &\quad \left.+\xi_2(L)\exp\left[\frac{\gamma z}{c}\left(\overline{\beta}_1(L)-\mathrm{i}\overline{\beta}_2(L)\right)\right]\right\} + c.c. \qquad (11)\end{aligned}$$

where $\overline{\beta}_1 = c\beta_1(L)/\gamma$, $\overline{\beta}_2 = c\beta_2(L)/\gamma$, are normalized quantities.

Using (11) into the boundary condition (3) we get

$$\begin{aligned}\delta\alpha^\lambda(0,t) &= (1-T)\mathrm{e}^{-\lambda\Delta t}\left\{\mu_1\exp\left[\frac{\gamma L}{c}\left(\overline{\beta}_1+\mathrm{i}\overline{\beta}_2\right)\right]\right.\\ &\quad \left.+\mu_2\exp\left[\frac{\gamma L}{c}\left(\overline{\beta}_1-\mathrm{i}\overline{\beta}_2\right)\right]\right\} \qquad (12)\end{aligned}$$

where μ_1 and μ_2 are given by

$$\begin{aligned}\mu_1 &= \mu_1(L,t) = \xi_1(L)\mathrm{e}^{\lambda t} \\ &= \frac{1}{2}\delta\alpha(0,t) - \frac{\mathrm{i}}{2\overline{\beta}_2} \\ &\quad \times \left\{\frac{1}{2}\left[\overline{C}_1(L) - \overline{C}_1^*(L)\right]\delta\alpha^{\lambda}(0,t) \right. \\ &\quad \left. + \overline{D}(L)\left(\delta\alpha^{\lambda}(0,t)\right)^*\right\} \end{aligned} \tag{13a}$$

and

$$\begin{aligned}\mu_2 &= \mu_2(L,t) = \xi_2(L)\mathrm{e}^{\lambda t} \\ &= \frac{1}{2}\delta\alpha(0,t) + \frac{\mathrm{i}}{2\overline{\beta}_2} \\ &\quad \times \left\{\frac{1}{2}\left[\overline{C}_1(L) - \overline{C}_1^*(L)\right]\delta\alpha^{\lambda}(0,t) \right. \\ &\quad \left. + \overline{D}(L)\left(\delta\alpha^{\lambda}(0,t)\right)^*\right\}. \end{aligned} \tag{13b}$$

Now we define the quantities

$$\begin{aligned}\eta_1 = \mathrm{e}^{\lambda\Delta t} &- \frac{1}{2}(1-T)\left\{\exp\left[\frac{\gamma L}{c}(\overline{\beta}_1 + \mathrm{i}\overline{\beta}_2)\right]\right. \\ &+ \exp\left[\frac{\gamma L}{c}(\overline{\beta}_1 - \mathrm{i}\overline{\beta}_2)\right] + \frac{\mathrm{i}}{2\overline{\beta}_2}\left[\exp\left[\frac{\gamma L}{c}(\overline{\beta}_1 - \mathrm{i}\overline{\beta}_2)\right]\right. \\ &\left.\left. - \exp\left[\frac{\gamma L}{c}(\overline{\beta}_1 + \mathrm{i}\overline{\beta}_2)\right]\right](\overline{C}_1 - \overline{C}_1^*)\right\} \end{aligned} \tag{14a}$$

and

$$\begin{aligned}\eta_2 = (1-T)&\frac{\mathrm{i}\overline{D}}{2\overline{\beta}_2} \\ &\times \left[\exp\left[\frac{\gamma L}{c}(\overline{\beta}_1 - \mathrm{i}\overline{\beta}_2)] - \exp[\frac{\gamma L}{c}(\overline{\beta}_1 + \mathrm{i}\overline{\beta}_2)]\right]\right]. \end{aligned} \tag{14b}$$

Hence from equations (12, 13) we have

$$\eta_1\delta\alpha^{\lambda}(0,t) = \eta_2\left(\delta\alpha^{\lambda}(0,t)\right)^*, \tag{15}$$

which means that

$$\eta_1 = \eta_2\mathrm{e}^{-2\mathrm{i}\phi_{\mathrm{f}}}. \tag{16}$$

From equations (14, 16) we then get

$$1 = \exp\left(-\frac{\gamma}{c}\overline{\lambda}\mathcal{L}\right)(1-T)\exp\left[\frac{\gamma L}{c}\left(\overline{B}_{\mathrm{r}} - \mathrm{i}\overline{\beta}_2\right)\right]\Omega \tag{17}$$

where

$$\begin{aligned}\Omega = \frac{1}{2}&\left\{1 + \exp\left[2\frac{\gamma L}{c}\mathrm{i}\overline{\beta}_2\right] + \frac{1}{\overline{\beta}_2}(-\overline{B}_{\mathrm{i}} + \mathrm{i}\overline{D}_1)\right. \\ &\left.\times\left[1 - \exp\left(2\frac{\gamma L}{c}\mathrm{i}\overline{\beta}_2\right)\right]\right\}, \end{aligned} \tag{18}$$

$\mathcal{L} = 2(\ell + L)$ and have used the relation $c\Delta t = 2\ell + L$, with $\overline{B}_{\mathrm{r}}$ and $\overline{B}_{\mathrm{i}}$ denote the real and imaginary parts of the normalized quantity $\overline{B}(\mathrm{L})$ and $\overline{D}_1 = \exp(-2\mathrm{i}\phi_{\mathrm{f}})\overline{D}$.

Equation (17) implies that

$$2\pi\mathrm{i}n = -\frac{\gamma}{2}\overline{\lambda}\mathcal{L} + \ln(1-T) + \frac{\gamma L}{c}(\overline{B}_{\mathrm{r}} - \mathrm{i}\overline{\beta}_2) + \ln(\Omega) \tag{19}$$

where $n = 0, \pm1, \pm2, \ldots$

For $T \ll 1$ (mean field limit), $\ln(1-T) \simeq -T$ and hence from (19) we have the generalised result

$$\overline{\lambda} = -\mathrm{i}\overline{\alpha}_n - \overline{k} + \frac{L}{\mathcal{L}}(\overline{B}_{\mathrm{r}} - \mathrm{i}\overline{\beta}_2) + \frac{c}{\gamma L}\ln(\Omega) \tag{20}$$

where $\overline{\alpha}_n = 2\pi nc/\gamma\mathcal{L}$ and $\overline{k} = Tc/\gamma\mathcal{L}$.

In the case of the normal vacuum ($N = |M| = 0$), equation (20) reduces to the result obtained in [3].

Note that $\overline{k}$ and the expression $L(\overline{B}_{\mathrm{r}} - \mathrm{i}\overline{\beta}_2)/\mathcal{L}$ are of order T (*cf.* Eq. (7)) and the expression $c\ln(\Omega)/(\gamma\mathcal{L})$ is of order T and higher (*cf.* Eq. (18)), and since both expressions $L(\overline{B}_{\mathrm{r}} - \mathrm{i}\overline{\beta}_2)/\mathcal{L}$ and $c\ln(\Omega)/(\gamma\mathcal{L})$ are functions of $\overline{\lambda}$ hence equation (20) can be evaluated to order T in the following single iteration form

$$\begin{aligned}\overline{\lambda} &= -\mathrm{i}\overline{\alpha}_n - \overline{k} + \frac{L}{\mathcal{L}}\left[\overline{B}_{\mathrm{r}}\left(\overline{\lambda} = \mathrm{i}\overline{\alpha}_n\right) - \mathrm{i}\overline{\beta}_2(\overline{\lambda} = \mathrm{i}\overline{\alpha}_n)\right] \\ &\quad + \frac{c}{\gamma L}\ln[\Omega(\overline{\lambda} = \mathrm{i}\overline{\alpha}_n)] \\ &\equiv F(\overline{\alpha}_n, |x|). \end{aligned} \tag{21}$$

The stationary solution is stable *if and only if* $\mathrm{Re}(\overline{\lambda}) \leq 0$ for all values of n. In the region where the curve $x = x(y)$ has a positive slope, the resonant mode ($n = 0$) is always stable but *some* of the off-resonant modes ($n \neq 0$) can become unstable.

We have numerically solved equation (21) for various set of the squeezed vacuum field parameters N and ϕ, and the output field $|x|$. We first present the numerical results of equation (21) in the normal vacuum ($N = M = 0$) in the case $\gamma_{\parallel} = 2\gamma_{\perp}$ in Figure 1. Note that from the OB curve, Figure 1a, the system is unstable for $x \in [1.1, 6.1]$ and stable elsewhere. For $|x| = 6.2, 7, 8$ and 9, one can find a region of $\overline{\alpha}_n$ in which $\mathrm{Re}(\overline{\lambda}) > 0$ (unstable solution) and elsewhere $\mathrm{Re}(\overline{\lambda}) \leq 0$ (stable solution), Figure 1b. For increasing $|x|$ the system becomes more stable as the positive $\mathrm{Re}(\overline{\lambda})$-range decreases, and the system is completely stable for $|x| = 9.9 \approx C/2$ as in [3] for $\gamma_{\parallel} = \gamma_{\perp}$. Alternatively, these results are presented in Figure 1c: on and outside the boundary of the island the region is stable ($\mathrm{Re}(\overline{\lambda}) \leq 0$) and inside the island it is unstable ($\mathrm{Re}(\overline{\lambda}) > 0$).

Now, in the squeezed vacuum case the results are presented in Figures 2–4. For $N = 0.1$, $|M|^2 = N(N+1)$ and $\phi = 0$, the system is unstable in the interval $|x| \in [1.8, 5.7]$, Figure 2. For $6 \leq |x| < 7$, the unstable region diminishes with increasing $|x|$ (Fig. 3). The result for $N = 0.1$ and $\phi = \pi/2$ shows the unstable region as an asymmetric island around $\overline{\alpha}_n = 0$ (Fig. 4).

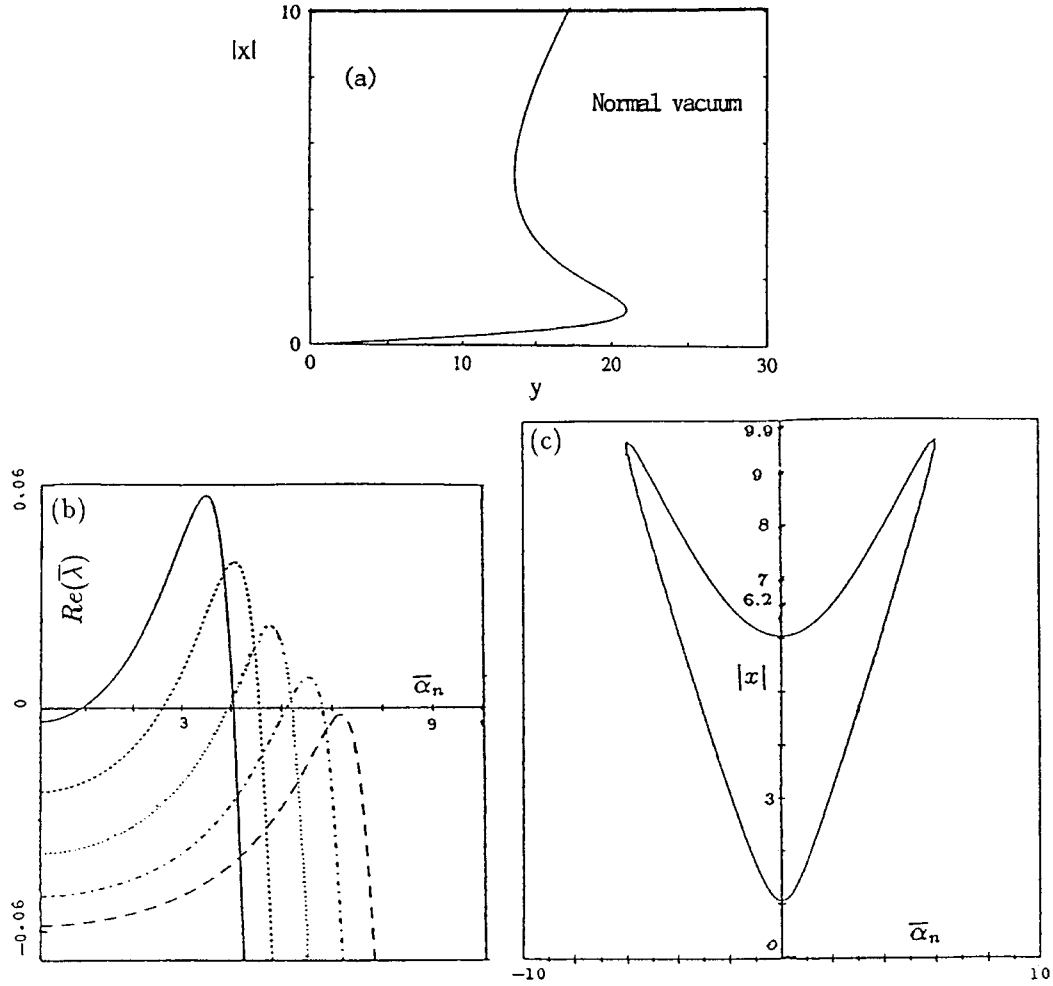

Fig. 1. (a) The characteristic relation between the transmitted intensity $|x|$ and the incident intensity y in the normal vacuum case ($N = M = 0$) for the absorptive case ($\theta = \delta = 0$) and $C = 20$. (b) $\overline{\alpha}_n$ *versus* $\mathrm{Re}(\overline{\lambda})$ for $\overline{k} = 0.1$ and $|x| = 6.2$ (——), $|x| = 7$ (----), $|x| = 8$ (· · · ·), $|x| = 9$ (– · – · –) and $|x| = 9.9$ (— —). (c) The unstable regions (inside the island) in the $(\overline{\alpha}_n, |x|)$-plane.

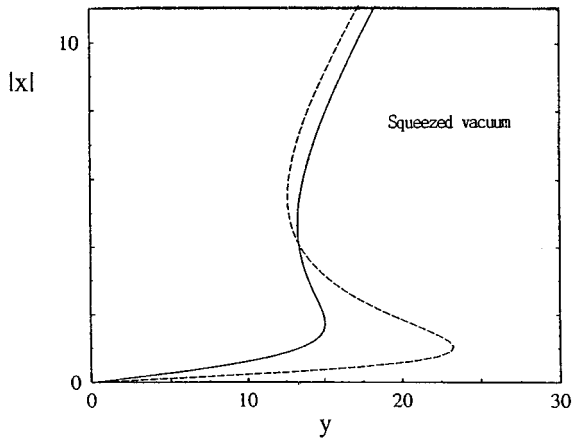

Fig. 2. The output intensity $|x|$ *versus* the input intensity y in the squeezed vacuum case for $N = 0.1$, $C = 20$ in the absorptive case ($\theta = \delta = 0$) and for $\phi = 0$ (——) and $\phi = \pi/2$ (– – –).

Now, for the stability of the system near the phase switching points: as we have seen in [1] for the absorptive case the effect of fixing the input coherent field y and changing the phase of the squeezed vacuum ϕ, the system shows (for $C > C_{\mathrm{crit}}^{\max}$ [1]) a one-way switching (*isola*) structure. For fixed $y = 13$ and at the switching-down point A ($|x| = 6.55$ and $\phi = 48°$) in Figure 5a, one finds the stationary solution is stable for certain values of $\overline{\alpha}_n$ (Figs. 5b and 5c). For the adjacent point B ($|x| = 7.2$ and $\phi = 40°$) in Figure 5a, the result in Figures 5d and 5e shows that the range for stable solution is wider than that at the point A. For fixed $y = 18$ and at the switching-up point A_1 ($|x| = 1.5$ and $\phi = 32°$) in Figure 6a the range of $\overline{\alpha}_n$ where the system is unstable, Figures 6b and 6c, is smaller compared with that in Figures 5b and 5c at the switching-down point A. As for the point B_1 ($|x| = 0.9$ and $\phi = 40°$) in Figure 6a the system shows no unstable behaviour for the positive off-resonant modes (Figs. 6d and 6e).

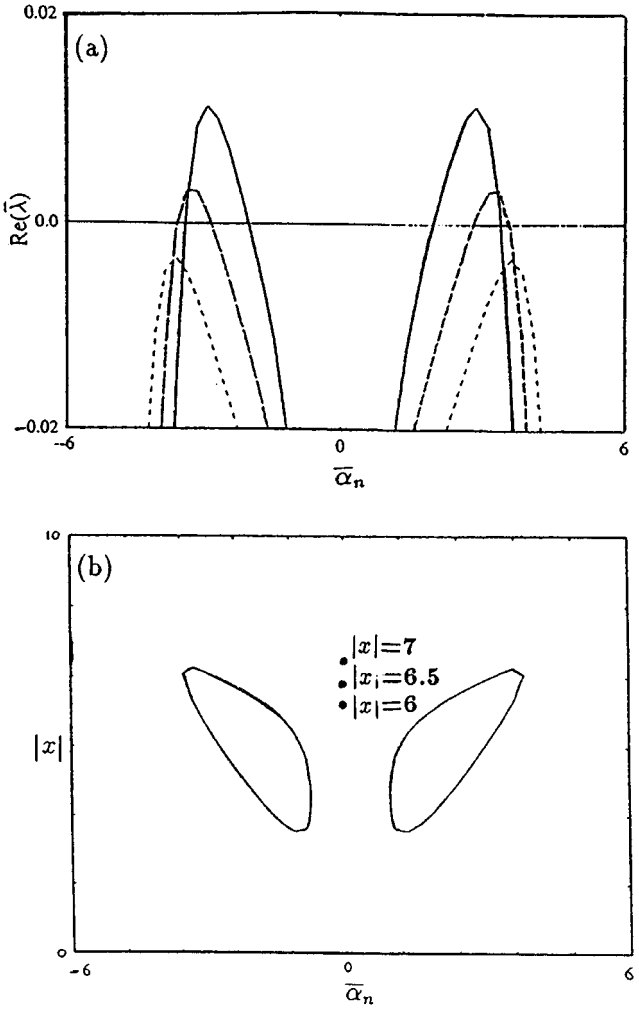

Fig. 3. (a) Same as Figure 1b but for $N = 0.1$, $\phi = 0$, $|x| = 6$ (——), $|x| = 6.5$ (- - -), and $|x| = 7$ (— —). (b) Same as Figure 1c but for $N = 0.1$, $\phi = 0$.

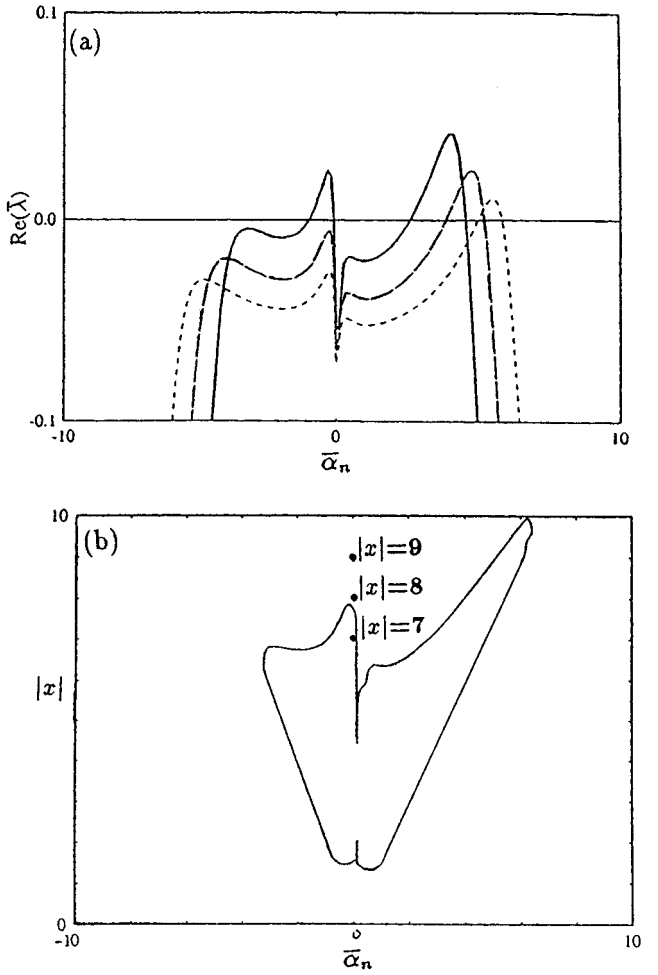

Fig. 4. (a) Same as Figure 3a but for $\phi = \pi/2$, $|x| = 7$ (——), $|x| = 8$ (- - -), and $|x| = 9$ (— —). (b) Same as Figure 3b but for $\phi = \pi/2$.

2.2 Dispersive case

For the homogeneous broadening case, the Maxwell-Bloch equations in the dispersive case (where either the atomic detuning δ or the cavity detuning θ or both are non-zero) describing the dynamics of the optical bistable system in squeezed vacuum are the same equations (1–3) but with G_o replaced by G [1],

$$G = \frac{\gamma}{2}\left(1 + 2N + \mathrm{i}\delta\right). \tag{22}$$

Following the same approach for the absorptive case but taking the boundary conditions for $\theta \neq 0$ (*cf.* Eqs. (1) of [1]) to be

$$\begin{aligned}\delta\alpha(0,t) &= (1-T)\delta\alpha(L, t-\Delta t)\exp(-\mathrm{i}\theta T)\\ &= |\delta\alpha(0,L)|\exp(\mathrm{i}\phi_{\mathrm{f}})\end{aligned} \tag{23}$$

where θ is the normalized cavity detuning. Hence equations (1–3, 22, 23) lead to an expression for $\overline{\lambda}$ *formally* similar to (21); *i.e.*

$$\begin{aligned}\overline{\lambda} = &-\mathrm{i}\overline{\alpha}_n - (1+\mathrm{i}\theta)\overline{k} + \frac{L}{\mathcal{L}}\left(\overline{B}_{\mathrm{r,d}} - \mathrm{i}\overline{\beta}_{2,\mathrm{d}}\right)\\ &+ \frac{\gamma L}{c}\ln(\Omega_{\mathrm{d}})\end{aligned} \tag{24}$$

where $\overline{B}_{\mathrm{r,d}}$ and $\overline{B}_{\mathrm{i,d}}$ are the real and imaginary parts of $\overline{B}_{\mathrm{d}}$. The quantities in (24) are given as follows,

$$\overline{B}_{\mathrm{d}} = -\Gamma_1\left\{\left(\overline{\lambda} + \overline{G}^*\right)\Gamma_2 - |x|^2\left(\overline{\lambda} + \overline{G}^* - |M|\mathrm{e}^{\mathrm{i}\phi}\right)\Gamma_3\right\}$$

$$\overline{\beta}_{2,\mathrm{d}} = \frac{c}{2}\left[|\overline{B}_{\mathrm{d}} - \overline{\lambda}|^2 - |\overline{D}_{1,\mathrm{d}}|^2 - (\mathrm{Re}(\overline{B}_{\mathrm{d}} - \overline{\lambda}))^2\right]^{\frac{1}{2}}$$

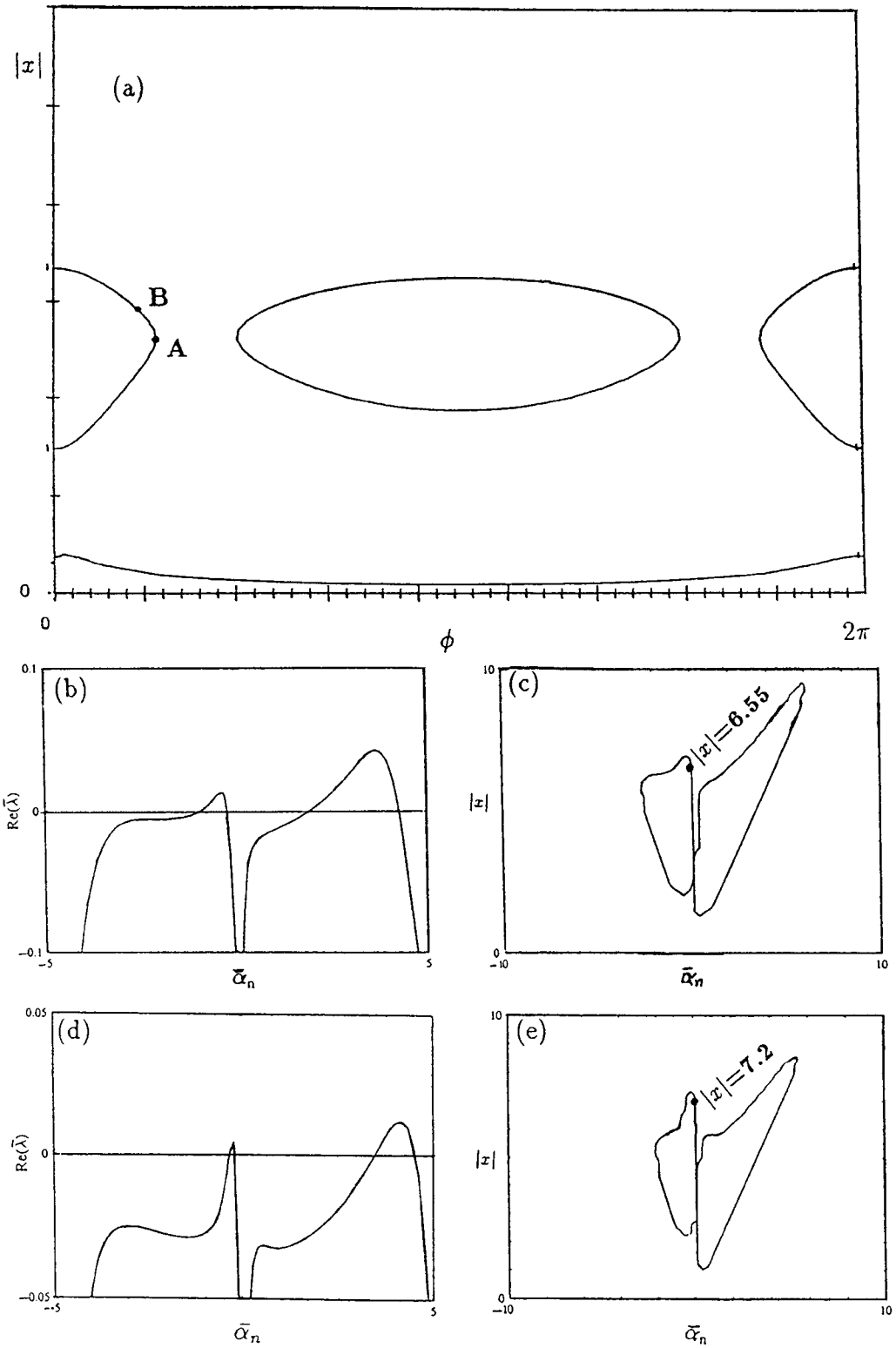

Fig. 5. (a) $|x|$ *versus* ϕ at fixed input value $y = 13$. The points A and B are ($|x| = 6.55$, $\phi = 48°$) and ($|x| = 7.2$, $\phi = 40°$) resp., (b) $\overline{\alpha}_n$ *versus* $\mathrm{Re}(\overline{\lambda})$ for $|x| = 6.55$ and $\phi = 48°$ ($N = 0.1$, $C = 20$, $\overline{k} = 0.1$ and $\theta = \delta = 0$). (c) $|x|$ *versus* $\overline{\alpha}_n$ for $\phi = 48°$. (d) Same as (b) but for $\phi = 40°$ and $|x| = 7.2$. (e) Same as (c) but for $\phi = 40°$.

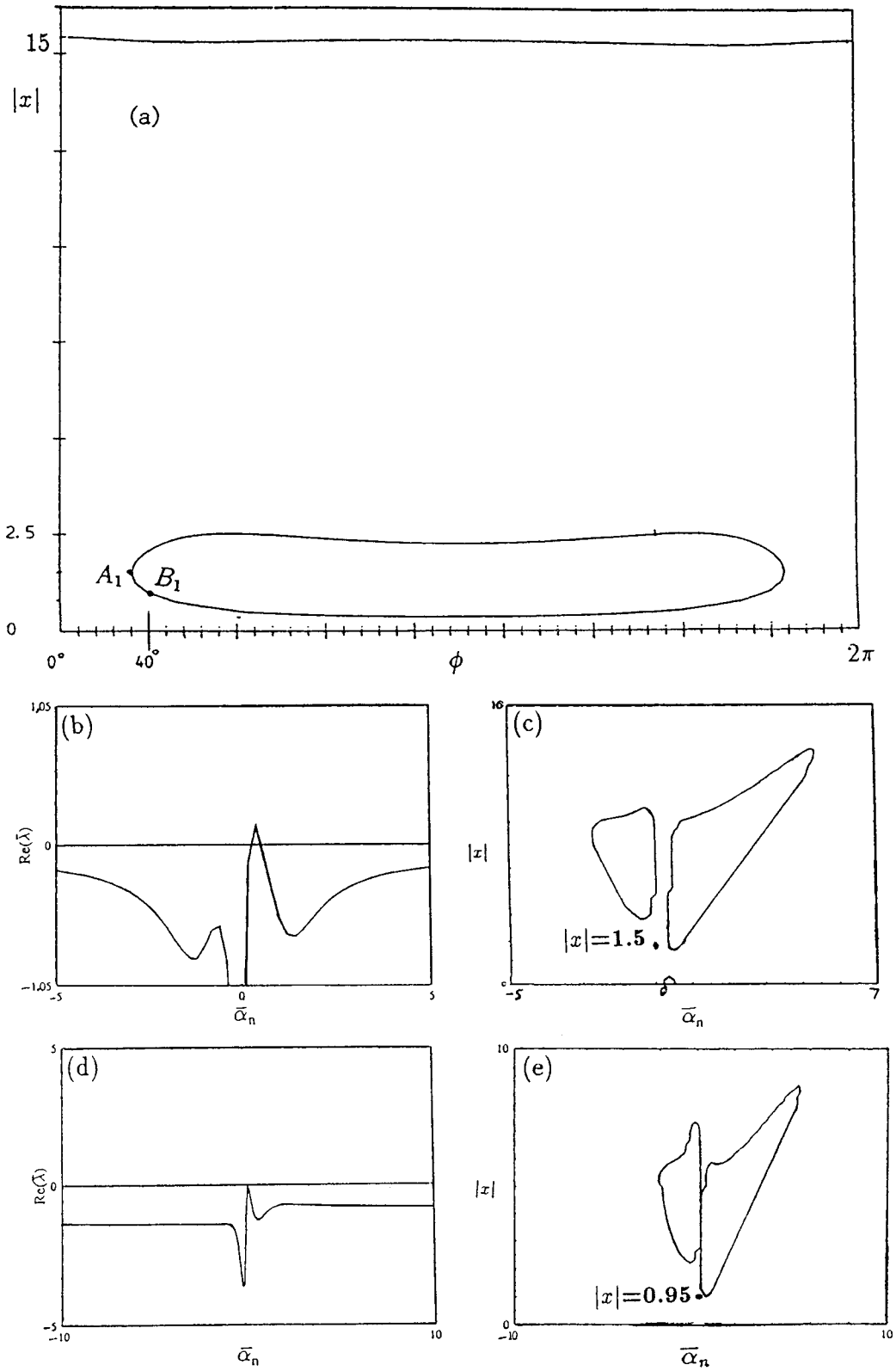

Fig. 6. (a) Same as Figure 5a but at $y = 18$. The points A_1 and B_1 are ($|x| = 1.5$, $\phi = 32°$) and ($|x| = 0.95$, $\phi = 40°$) resp., (b) same as Figure 5b but for $|x| = 1.5$ and $\phi = 32°$. (c) Same as Figure 5c but for $\phi = 32°$. (d) Same as Figure 5b but for $|x| = 0.95$ and $\phi = 40°$. (e) Same as Figure 5c but for $\phi = 40°$.

and

$$\Omega_{\rm d} = \frac{1}{2}\Bigg\{1+\exp\left[2\frac{\gamma L}{c}{\rm i}\overline{\beta}_{2,{\rm d}}\right] + \frac{1}{\overline{\beta}_{2,{\rm d}}}\left(-\overline{B}_{{\rm i},{\rm d}}+{\rm i}\overline{D}_{1,{\rm d}}\right)\left[1-\exp\left(2\frac{\gamma L}{c}{\rm i}\overline{\beta}_{2,{\rm d}}\right)\right]\Bigg\},$$

$$\overline{D}_{1,{\rm d}} = \Gamma_1\left[|M|{\rm e}^{{\rm i}\phi}\Gamma_2+|x|^2\left(\overline{\lambda}+\overline{G}^*-|M|{\rm e}^{{\rm i}\phi}\right)\Gamma_3^*\right],$$

$$\overline{G} = G/\gamma,$$

$$\Gamma_1 = (1+2N)^{-1}(|\overline{\lambda}+\overline{G}|^2-|M|^2)^{-1} \times\left(1+\frac{b_1\,|x|^2}{1+\delta^2}\right)^{-1}\Gamma_2^{-1},$$

$$\Gamma_2 = \overline{\lambda}+1+2N+\frac{1}{4}|x|^2\frac{2\overline{\lambda}+b_1(1+2N)}{|\overline{\lambda}+\overline{G}|^2-|M|^2},$$

$$\Gamma_3 = (1+\delta^2)^{-1}\left(\overline{G}-|M|{\rm e}^{-{\rm i}\phi}\right)+\frac{1}{4}\frac{\overline{\lambda}+\overline{G}^*-|M|{\rm e}^{-{\rm i}\phi}}{|\overline{\lambda}+\overline{G}|^2-|M|^2}\cdot \tag{25}$$

From equation (24) we notice that the change of the cavity detuning θ has no direct effect in finding a stable stationary solutions but it has an indirect *via* the values of the output field $|x|$. In general, $\mathrm{Re}(\overline{\lambda})>0$ corresponds to the points of the curve $x(y)$ with negative slope, so that all these points are unstable while for points of the positive slope with $\mathrm{Re}(\overline{\lambda})<0$ at $n=0$, the resonant mode is always stable there.

In the squeezed vacuum case the results are presented in Figures 7–9. First, for the squeezed parameter $N=0.1$, $|M|^2=N(N+1)$, $C=40$, $\theta=\delta=5$ and $\phi=0$, the system is unstable in the interval $|x|\in[5,9.25]$, Figure 7. For $30\le|x|\le 90$ the region of $\overline{\alpha}_n$ where $\mathrm{Re}(\overline{\lambda})$ is positive decreases with increasing $|x|$, Figure 8a. The results for $\phi=\pi/2$ (Fig. 9) are qualitatively similar but with separated unstable areas around $|x|\simeq 60$ (Fig. 9b). In general, the region where $\mathrm{Re}(\overline{\lambda})>0$ (the area inside the *stick-shape* curve, Figs. 8b and 9b) is smaller compared with the absorptive case (Figs. 3b, 5c, 5e, 6c and 6e). We also note that in the dispersive case the unstable stationary solutions (*i.e.* $\mathrm{Re}(\overline{\lambda})>0$) exist for positive values of $\overline{\alpha}_n$ only. Also by fixing $|x|$ the range of $\overline{\alpha}_n$ for which $\mathrm{Re}(\overline{\lambda})>0$ decreases as ϕ increases.

3 Self-pulsing and chaos

The linear stability analysis around the stationary state in the previous section shows that, under certain conditions and for some values of the system parameters, part of the upper branch of the bistable curve can be unstable. What happens next is the following. The system (in this unstable region of the upper branch) either precipitates to the low transmission branch or exhibits oscillatory behaviour. Note that this oscillatory behaviour is *spontaneously* produced in the sense that all the external (Master) parameters are kept fixed. The analytical study of the

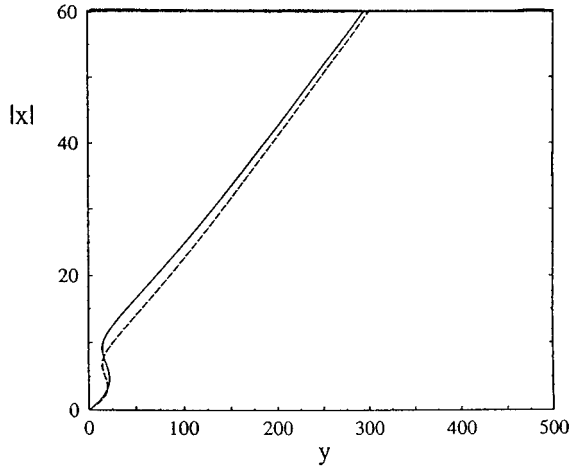

Fig. 7. $|x|$ *versus* y for $C=40$, $N=0.1$, $\theta=\delta=5$, $\phi=0$ (——) and $\phi=\pi/2$ (– – –).

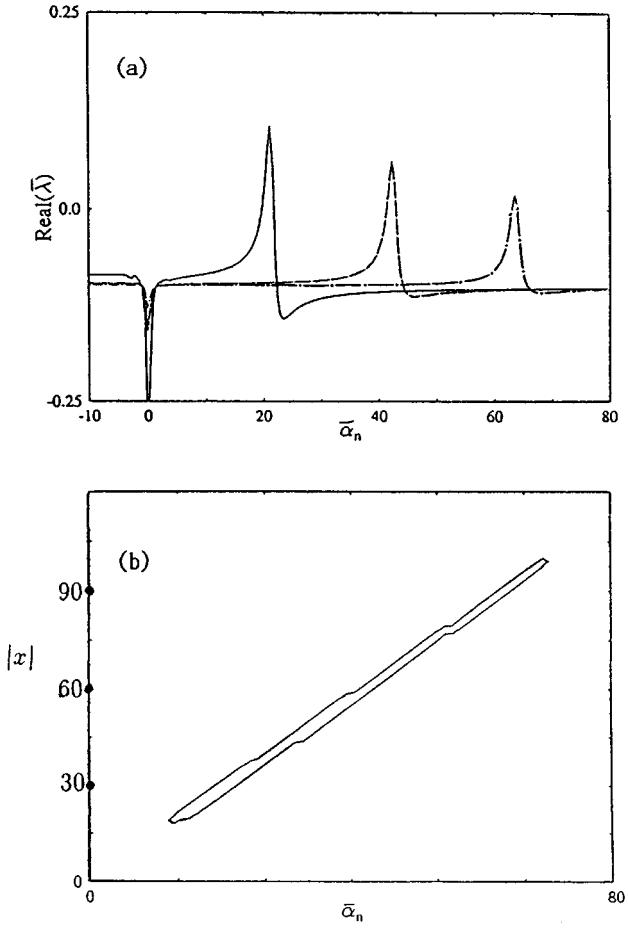

Fig. 8. (a) $\overline{\alpha}_n$ *versus* $\mathrm{Re}(\overline{\lambda})$ for $C=40$, $N=0.1$ $\delta=5$, $\phi=0$, $|x|=30$ (——), $|x|=60$ (– – –) and $|x|=90$ (– · – · –). (b) $|x|$ *versus* $\overline{\alpha}_n$ for $C=40$, $N=0.1$, $\delta=5$ and $\phi=0$.

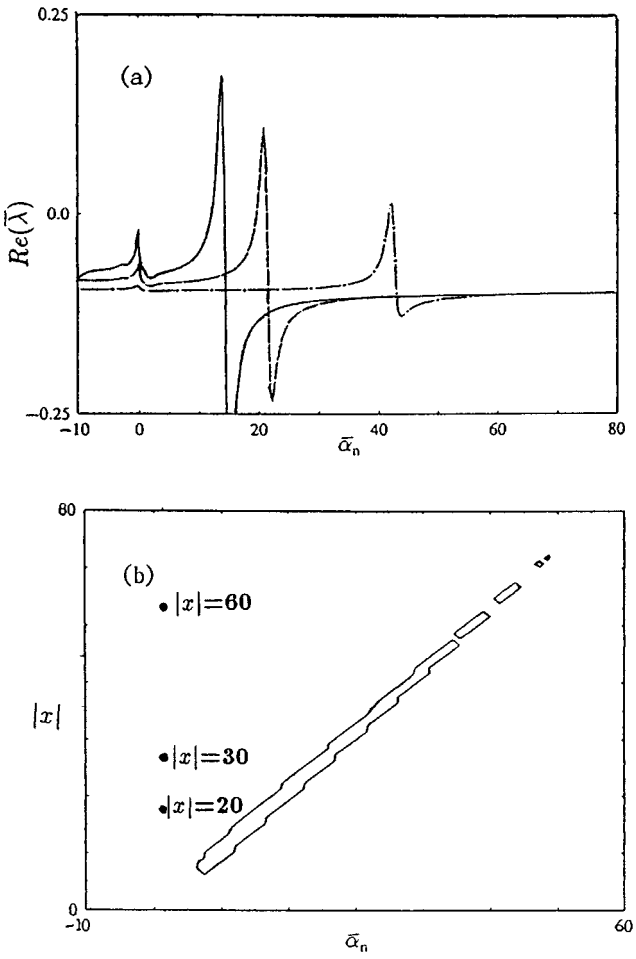

Fig. 9. (a) Same as Figure 8a but for $\phi = \pi/2$, $|x| = 20$ (——), $|x| = 30$ (— — —) and $|x| = 60$ (—·—·—). (b) Same as Figure 8b but for $\phi = \pi/2$.

instability (*cf.* [6]) for absorptive and dispersive bistability in the normal vacuum shows that the instability of the upper positive slope branch may exist if at least one of the off-resonant modes is unstable. There are, essentially, different three types of unstable behaviour:

(1) *bifurcation* behaviour which means transition in a continuous way to a new steady state,
(2) *self-pulsing oscillatory* behaviour which is a non-stationary periodic behaviour in time,
(3) *chaotic* behaviour which is a non-stationary behaviour *but* not periodic in time.

In this section we investigate the self-pulsing and chaotic behaviour for the model equations (2) in reference [1] in the dispersive case (since this is more prominent than the absorptive case, as in the normal vacuum case [4]).

Within the mean field limit, we integrate the field equation, equation (2a) of [1] with respect to z and use the boundary conditions equations (1) of [1]. The result is

$$\frac{\mathrm{d}\overline{\alpha}}{\mathrm{d}t} = -\mathrm{i}k\theta\overline{\alpha} - k(\overline{\alpha} - E_I) - gn_0\overline{J}_-. \qquad (26a)$$

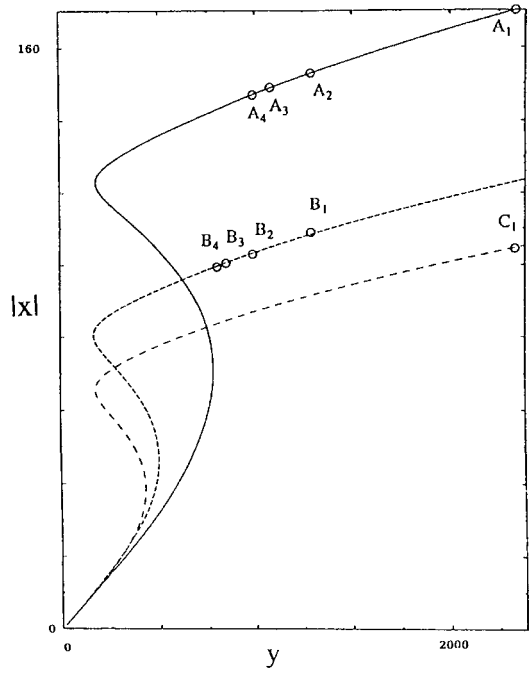

Fig. 10. $|x|$ *versus* y for $C = 80\,000$, $N = 0.1$, $\delta = 374$, $\theta = 340$ and for $\phi = 0$ (——), $\phi = \pi/2$ (- - - -) and $\phi = \pi$ (— —).

When the equations of the atomic variables (Eqs. (2b, 2c)) of [1]) are spatially integrated in the mean field limit, we get

$$\frac{\mathrm{d}\overline{J}_-}{\mathrm{d}t} = -G\overline{J}_- + 2g\overline{\alpha}\overline{J}_z - \gamma M\overline{J}_+ = \left(\frac{\mathrm{d}\overline{J}_+}{\mathrm{d}t}\right)^* \qquad (26b)$$

$$\frac{\mathrm{d}\overline{J}_z}{\mathrm{d}t} = -\gamma_\parallel\overline{J}_z - \frac{1}{2}\gamma - g(\overline{\alpha}\overline{J}_+ + \overline{\alpha}^*\overline{J}_-) \qquad (26c)$$

where $k = c/\mathcal{L}$ is the cavity damping coefficient and the time-dependent variables $\overline{\alpha}$, $\overline{J}_\pm$, $\overline{J}_z$ are space-averaged quantities, $\overline{\alpha} = L^{-1}\int_0^L \alpha(z,t)\mathrm{d}z$, etc. Now, we examine the dynamical behaviour of the model equations (26) in the two cases of adiabatic and non-adiabatic regimes.

3.1 Adiabatic behaviour

Here it is assumed that the relaxation time $\gamma_\perp^{-1}$ for the polarization components $J_\pm$ is the shortest of all the other characteristic times ($\gamma_\perp \gg \gamma_\parallel$, k, $k\theta$, kC). Hence by substituting in equations (26), for $J_\pm$ by their stationary values given by (1b), and by putting the normalised output field $x(t) = u + \mathrm{i}v$ we reach the following reduced system of ordinary differential equations,

$$\begin{aligned}\bar{k}\,\frac{\mathrm{d}J_z}{\mathrm{d}\tau} = &-\frac{1}{2} - (1+2N)J_z - \frac{1}{4}J_z \\ &\times \left[\frac{1}{4}\left((1+2N)^2 + \delta^2\right) - |M|^2\right]^{-1} \\ &\times \left\{(1+2N)(u^2+v^2) - 2|M| \right. \\ &\left. \times \left[(u^2-v^2)\cos(\phi) + 2uv\sin(\phi)\right]\right\} \qquad (27)\end{aligned}$$

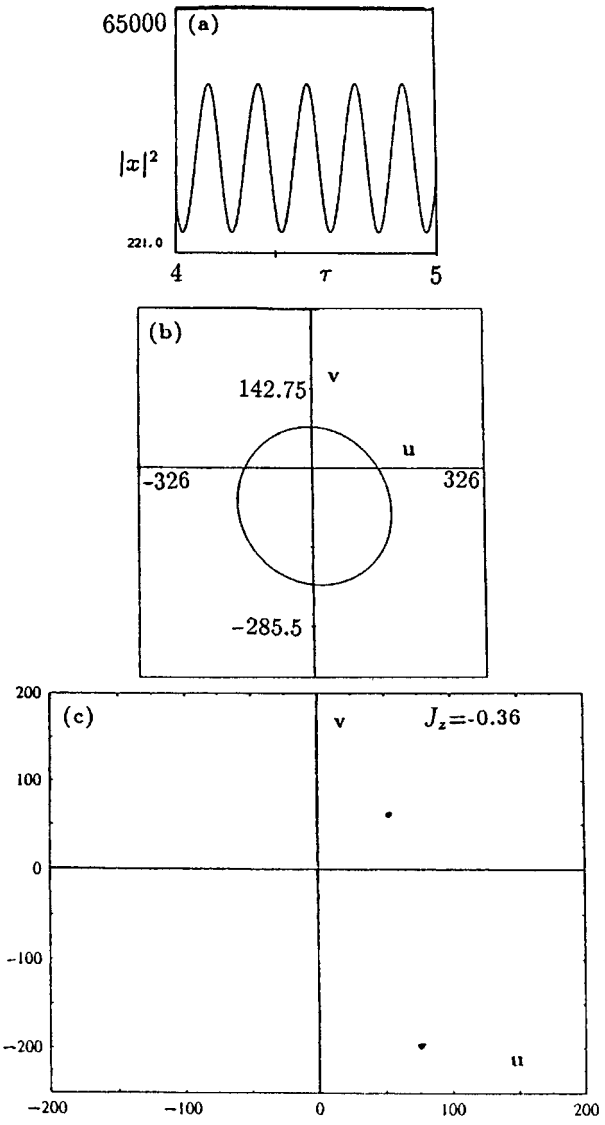

Fig. 11. The case of $C = 80\,000$, $N = 0.1$, $\theta = 340$, $\delta = 374$, $\overline{k} = 1/4$ and $\phi = 0$. (a) The output intensity $|x|^2$, at fixed $y = 2334$ (point A_1 in Fig. 10), *versus* the dimensionless time τ. (b) The corresponding phase space (u, v)-plane. (c) Poincaré map of the solution at $J_z = -0.36$.

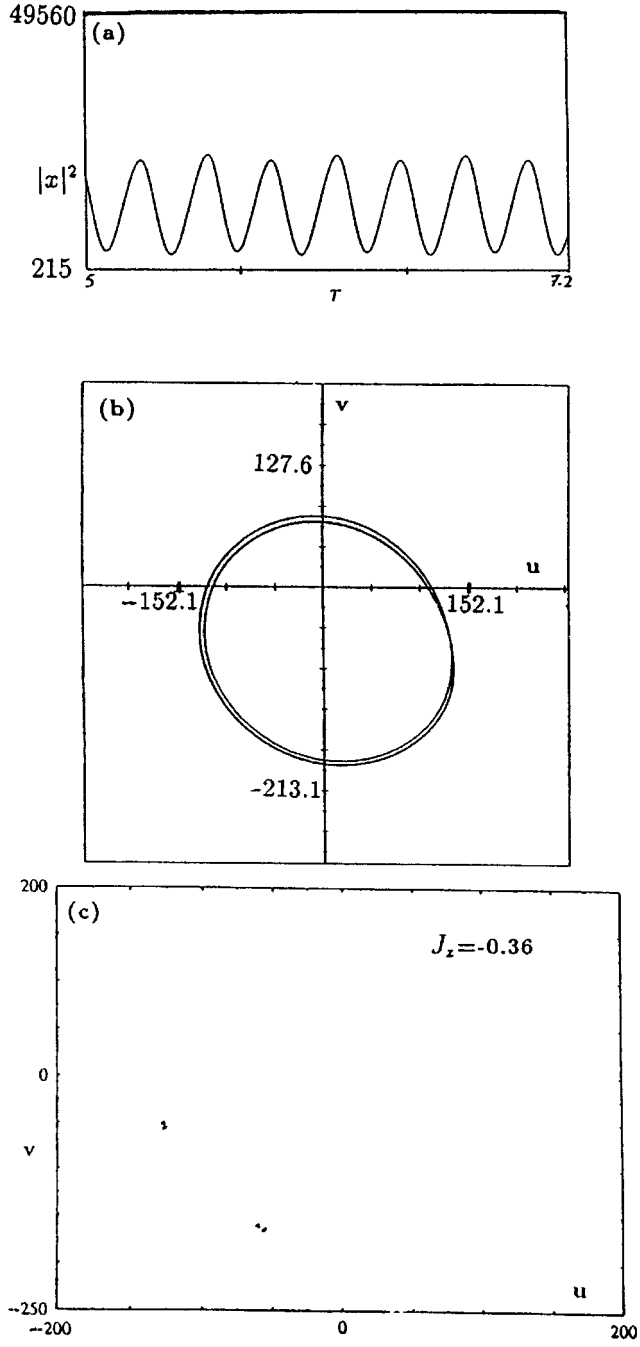

Fig. 12. Same as Figure 11 but for $y = 1293$.

$$\frac{\mathrm{d}u}{\mathrm{d}\tau} = \theta v - u + y + 2CJ_z \times \left[\frac{1}{4}\left((1+2N)^2 + \delta^2\right) - |M|^2\right]^{-1} \times \left[\frac{1}{2}(1+2N)u + \frac{1}{2}v\delta - |M|\,(u\cos(\phi) + v\sin(\phi))\right] \quad (28)$$

$$\frac{\mathrm{d}v}{\mathrm{d}\tau} = -\theta u - v + 2CJ_z \left[\frac{1}{4}\left((1+2N)^2 + \delta^2\right) - |M|^2\right]^{-1} \times \left[\frac{1}{2}(1+2N)v - \frac{1}{2}u\delta - |M|\,(u\sin(\phi) - v\cos(\phi))\right] \quad (29)$$

where $\overline{k} = k/\gamma$, $\tau = kt$. Now we present the numerical integration of the system (27–29) for the output field $x = u + \mathrm{i}v$ for the set of parameters $\theta = 340$, $\delta = 374$, $C = 80\,000$, $\overline{k} = 1/4$ (as in the normal vacuum case [7]) and for squeezed vacuum field parameters $N = 0.1$ and $\phi = 0$, $\pi/2$, π. The steady state OB curves in this case are shown in Figure 10.

In the case of $\phi = 0$ and for the control parameter $|y| = 2334$ (point A_1 in Fig. 10) the result for the output intensity $|x|^2$ against τ shows stable regular oscillations, Figure 11a, and only one loop in the (u, v)-plane,

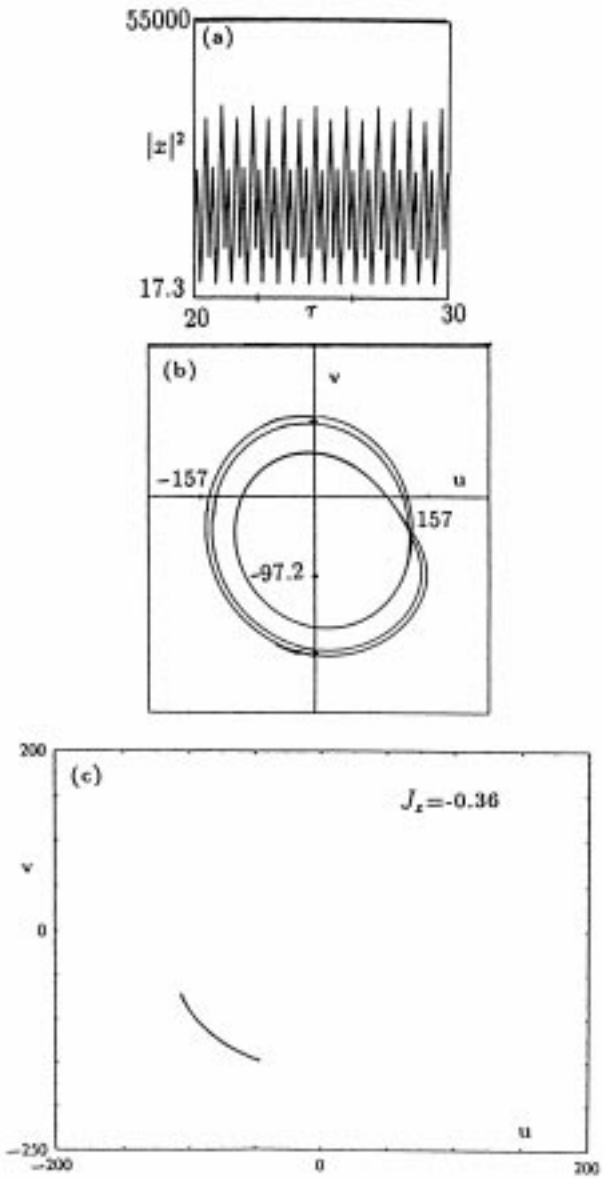

Fig. 13. Same as Figure 11 but for $y = 1080.2$.

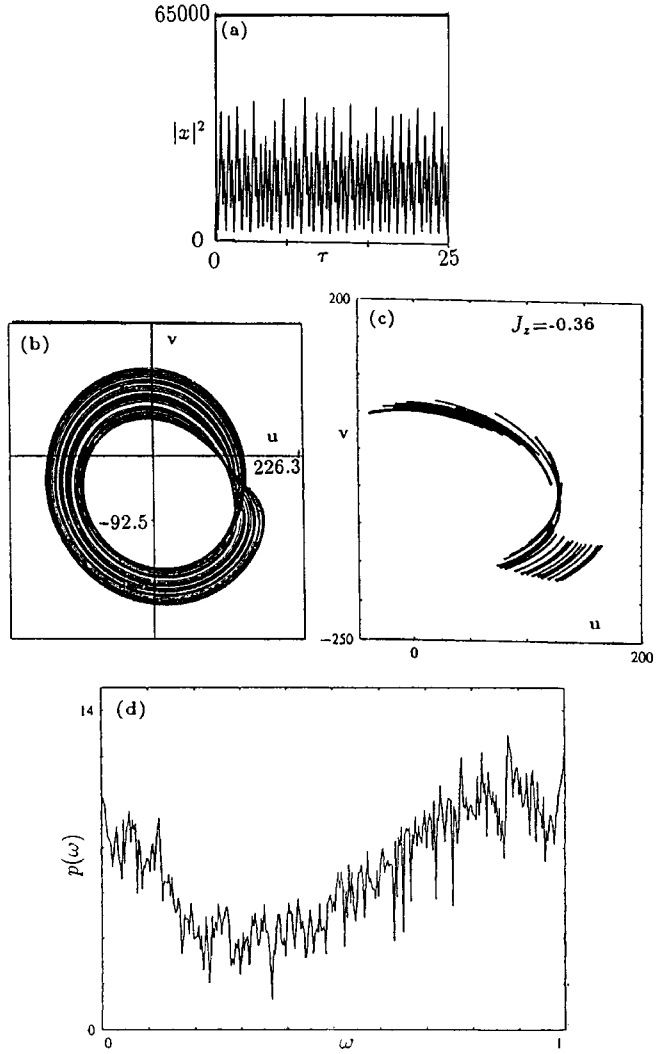

Fig. 14. (a–c) Same as Figures 11a–11c but for $y = 990$. (d) The power spectrum of the output intensity *versus* the frequency.

Figure 11b, with the Poincaré map shown in Figure 11c. For decreasing values of $|y|$ (points A_2 and A_3 in Fig. 10) the stable regular oscillations become unstable and the system approaches a new oscillatory state with period doubling with two loops in Figure 12 and four loops in Figure 13b. For a further decrease of $|y| = 990$ (point A_4 in Fig. 10) the oscillations become aperiodic and the system shows then a chaotic behaviour, Figure 14, where the power spectrum $P(\omega)$ (Fourier transform of $|X(t)|^2$) is shown in Figure 14d.

For $\phi = \pi/2$, similar results are obtained at the points $B_1 - B_3$ in Figure 10 and the chaotic behaviour at the point B_4 is similar to that of $\phi = 0$ (Figs. 14a–14d) but the phase-space contours and the Poincaré map are slightly different; Figures 15a–15d.

As for the case of $\phi = \pi$ and for $|y| = 2334$ (point C_1 in Fig. 10) the results [8] showed a one-loop oscillatory behaviour. Note that for the values of $|y|$ less than or greater than 2334 on the upper branch, the output field intensity decays (and the single loop becomes a single point in the (u, v)-plane) which is a manifestation of the system precipitating to the lower branch.

3.2 Non-adiabatic behaviour

In this case the full model equations of (26) for the field (α and α^*) and the atomic variables $J_{z,\pm}$ are solved numerically (using the Runge-Kutta Merson method). For the same set of parameters as in the adiabatic regime the results are presented in Figures 16 and 17. Figure 16a represents the time dependent behaviour for the output intensity $|x|^2 = u^2 + v^2$ *versus* the dimensionless time τ, while Figure 16b represents the 3-dimensional trajectory (u, v, J_z)-plane and Figure 16c represents the Poincaré map of the fixed plane, $J_z = -0.0545$. The phase-space

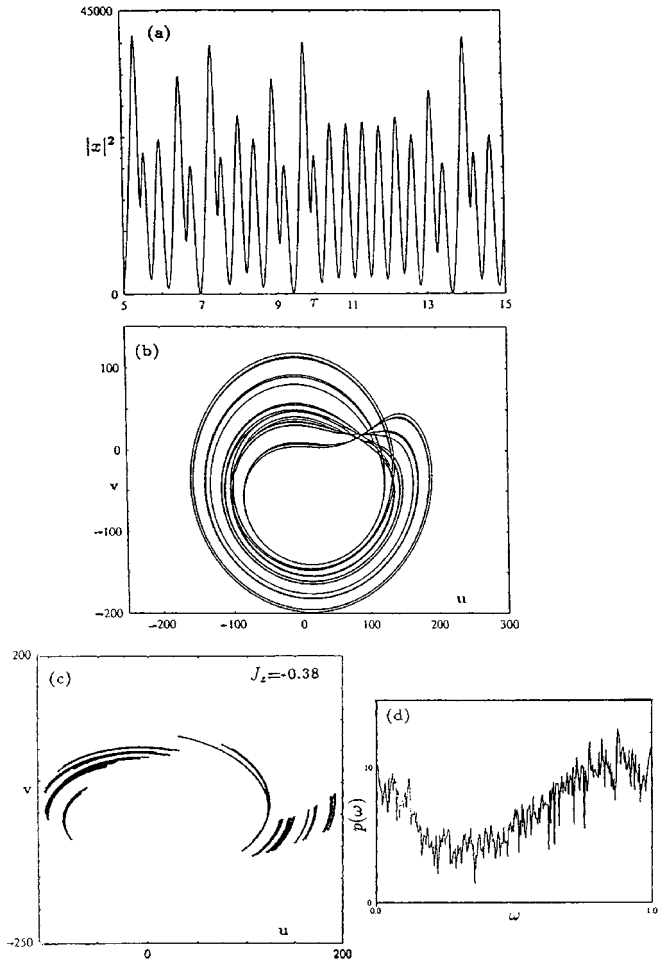

Fig. 15. Same as Figure 14 but for $\phi = \pi/2$ and $y = 802$.

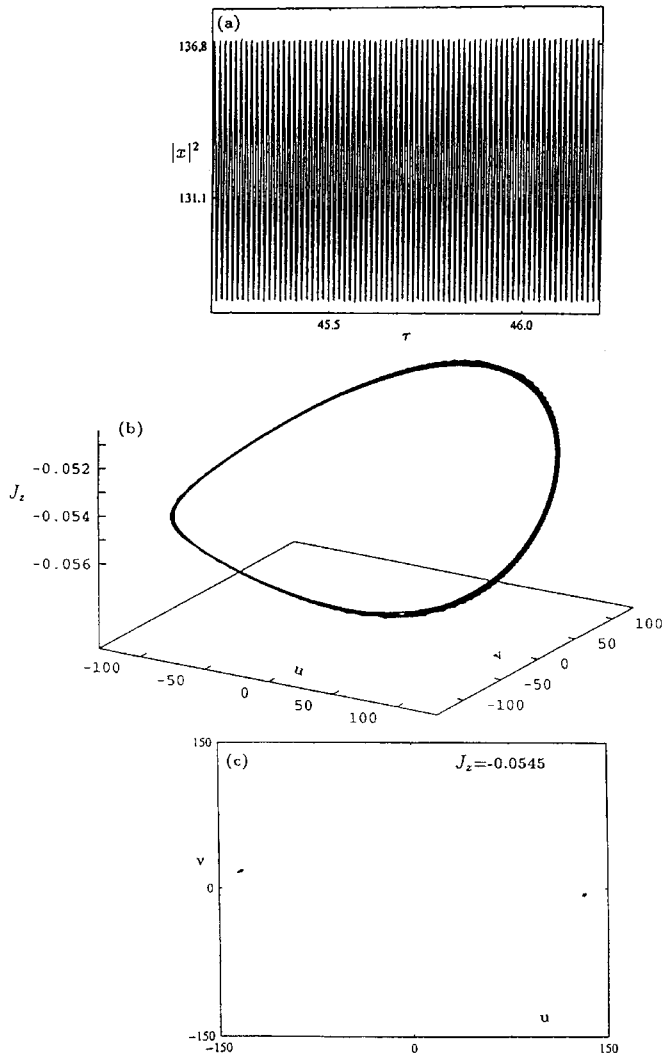

Fig. 16. The case of $C = 80\,000$, $N = 0.1$, $\theta = 340$, $\delta = 374$, $y = 2334$ and $\phi = 0$. (a) The output intensity $|x|^2$ (point A_1 in Fig. 10) *versus* the dimensionless time τ. (b) The 3-dimensional trajectory (u, v, J_z)-plane. (c) The corresponding Poincaré map of the solution at $J_z = -0.0545$.

diagram (Figs. 17) shows that the system exhibits a higher-order quasi-periodic behaviour, as a result of a higher-order system structure [9]. It shows a two-periodic behaviour lies on a two-torus. In this two-periodic trajectory, if the simulations were run longer, it becomes more densely filled in, Figure 17b. For $|y| = 2334$ (point A_1 in Fig. 10) the number of oscillations is 80, Figure 17a, and as $|y|$ decreases to be 1293 and 1080.2 (points A_2 and A_3 in Fig. 10) the number of oscillations decreases to be 53 and 50 (figures similar to Fig. 17a). For $|y| = 990$ (point A_4 in Fig. 10) the number of oscillations becomes 97. As for $\phi = \pi/2$, $y = 1293$, 990, 850 and 802 (points $B_1, ..., B_4$ in Fig. 10) we find that the number of oscillations decreases to be 74, 57, 53, and 53 with no increase at the point B_4 as happened at A_4. For $\phi = \pi$ and $y = 2334$ the number of oscillations becomes 52 (note that we have presented only the figures for the case $\phi = 0$, but similar pattern essentially is found for other values of ϕ [8]).

4 Summary

We have presented a linear stability analysis of the Maxwell-Bloch equations modelling a bistable system in a ring cavity configuration and in contact with a squeezed vacuum field. The investigation presented generalise earlier work in the normal vacuum case (*cf.* [6]). The squeeze phase parameter induces an asymmetry in the structure of the unstable region compared with the normal vacuum case. Also, the stability of the solution has been examined near the "phase switching-up and -down" points where we have found a stable solution for some of the off-resonant modes. The self-pulsing behaviour for the system was examined in both the adiabatic and non-adiabatic regimes. The structure of the self-oscillations *via* period doubling and its termination to chaotic behaviour for certain range of the system parameters were examined in detail. Specifically, in the non-adiabatic regime the phase-space diagram shows that the system exhibits a higher-order quasi-periodic behaviour which lies on a two-torus.

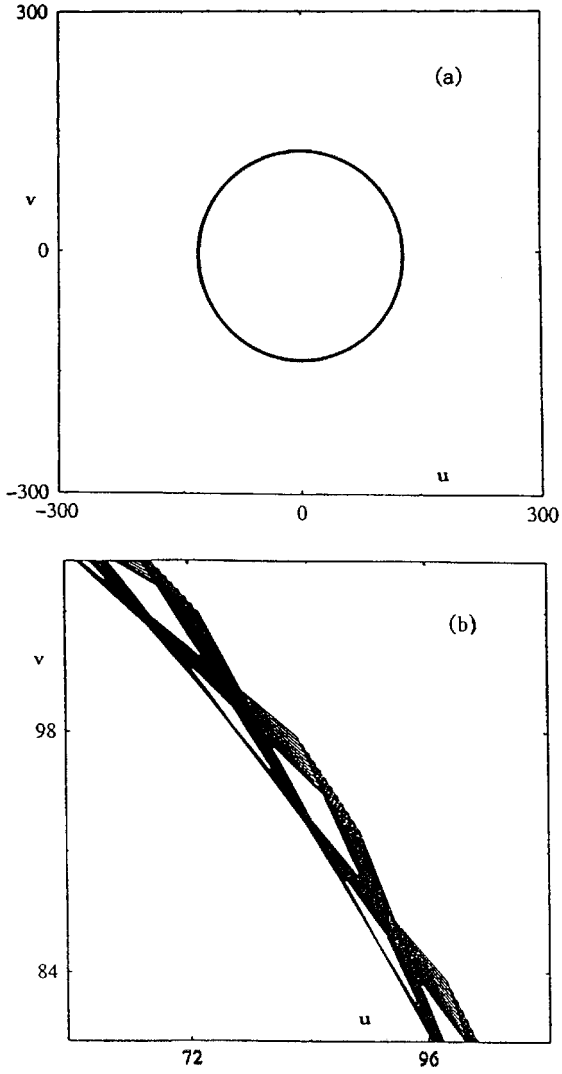

Fig. 17. (a) The phase-space, (u, v)-plane, for $C = 80\,000$, $N = 0.1$, $\theta = 340$, $\delta = 374$ and $y = 2334$. (b) A zoom view at a part of the (u, v)-plane.

In general, the study presented here for the non-linear dynamical system of OB with squeezed vacuum field inputs has its *relevance and importance* to the recent field of interest for optical scientists in the identification of chaos and its use in optical communications. For example, chaotic laser signals in communications is used to generate complex signals needed in the current complex systems as it can be used to synchronize a transmitter and receiver to transmit encrypted data [10]. Similar synchronization of chaotic behaviour in non-linear biological systems is used to exhibit stable cycles of gene activity (*i.e.* healthy life) [11]. Also, chaotic patterns are used to develop a data-coding scheme in signal communication coding algorithm, *e.g.* to ease crowding on the airwaves [12].

References

1. S.S. Hassan, H.A. Batarfi, R. Saunders, R.K. Bullough, Eur. Phys. J. D **8**, 403 (2000).
2. S.L. McCall, Appl. Phys. Lett. **32**, 284 (1978).
3. R. Bonifacio, L.A. Lugiato, Lett. Nouvo Cimento **21**, 510 (1978).
4. R. Bonifacio, M. Gronchi, L.A. Lugiato, Opt. Commun. **30**, 129 (1979).
5. L.A. Lugiato, Opt. Commun. **33**, 108 (1980).
6. L.A. Lugiato, L.M. Naducci, in *Fundamental systems in Quantum Optics*, edited by J. Dalibard, J.M. Raimond, J. Zinn-Justin (Elsevier Sci. Publ., Amsterdam, 1992), pp. 942-1047.
7. L.A. Lugiato, L.M. Narducci, D.K. Brandy, C.A. Pennise, Opt. Commun. **43**, 281 (1982).
8. H.A. Batarfi, Ph.D. thesis, University of Manchester, 1995.
9. T.S. Parker, L.O. Chua, *Practical Numerical Algorithms For Chaotic Systems* (Springer-Verlag, NY, 1989).
10. G.D. van Wiggeren, R. Roy, Science **279**, 1198 (1998); L. Pecora, Phys. World **11**, 25 (April, 1998).
11. S.A. Kauffman, Scientific American **264**, 64 (August, 1991).
12. E. Corcoran, Scientific American **264**, 82 (August, 1991).